The Thesis Committee for Feng Wen
Certifies that this is the approved version of the following thesis:

Shell Morphology and Raman Spectra of Epitaxial Ge−Si_xGe_{1-x} and Si−Si_xGe_{1-x} Core-Shell Nanowires

APPROVED BY
SUPERVISING COMMITTEE:

Supervisor:

Emanuel Tutuc

Edward T. Yu

Shell Morphology and Raman Spectra of Epitaxial Ge−Si_xGe_{1-x} and Si−Si_xGe_{1-x} Core-Shell Nanowires

by

Feng Wen

Thesis

Presented to the Faculty of the Graduate School of

The University of Texas at Austin

in Partial Fulfillment

of the Requirements

for the Degree of

Master of Science in Engineering

The University of Texas at Austin

May 2018

Acknowledgements

I would like to thank all who help me through writing this thesis.

In particular, I want to express my sincere gratitude to my advisor, Prof. Emanuel Tutuc. His unfailing guidance and thoughtful critiques of my work, combined with his extensive knowledge in this field, has paved my way to become a better student and researcher. I also want to thank Dr. Edward Yu for his time and feedback as a reader of this thesis.

I also want to thank my previous and current groupmates helping me with either experiment facility use or discussion of my research. Babak, Kayoung, Kyoung and Stefano have all offered me great help. Foremost, David, his mentorship has greatly accelerated my learning speed. He not only trains me on most relevant experimental tools, but helps me learn important backgrounds and analysis skills as well. In addition, thanks to his excellent work, I can take a lot of things for granted to focus on unexplored part of my research topic.

The hard work of technicians and administrators allows me to focus on my research work. I want to thank Ricardo, Bill, Jesse, Johnny, James, Gerlinde, Joyce and Christine for this.

Constant help and support of my parents over the years enable me to go this far, I want to express my best gratitude and love to them. I also want to thank my amazing and beautiful wife Hehui for being my companion and keeping me happy all the time.

Abstract

Shell Morphology and Raman Spectra of Epitaxial Ge−Si_xGe_{1-x} and Si−Si_xGe_{1-x} Core-Shell Nanowires

Feng Wen, M.S.E.

The University of Texas at Austin, 2018

Supervisor: Emanuel Tutuc

In this thesis, we investigate the shell morphology and Raman spectra of epitaxial Ge−Si_xGe_{1-x} and Si−Si_xGe_{1-x} core−shell nanowire heterostructures grown using a combination of vapor−liquid−solid (VLS) growth mechanism for the core, followed by in-situ epitaxial shell growth using ultra-high vacuum chemical vapor deposition. Cross-sectional transmission electron microscopy reveals that the VLS growth yields cylindrical Ge and Si nanowire cores, growing along the <111> and <110> or <112> directions, respectively. A hexagonal cross-sectional morphology is observed for Ge-Si_xGe_{1-x} core-shell nanowires terminated by six {112} facets. Two distinct morphologies are observed for Si-Si_xGe_{1-x} core-shell nanowires that are either terminated by four {111}, and two {100} planes associated with <110> growth direction, or four {113}, and two {111} planes associated with <112> growth direction. We show that the Raman spectra of Si- Si_xGe_{1-x}

is correlated with the shell morphology thanks to epitaxial growth-induced strain, with the core Si-Si mode showing a larger red shift in <112> core-shell nanowires compared to their <110> counterparts. We compare the Si-Si Raman mode value with calculations based on a continuum elasticity model coupled with lattice dynamic theory.

Table of Contents

Acknowledgement iii

List of Tables viii

List of Figures ix

Chapter 1 Introduction 1

1.1 Motivation and Thesis Highlight 1

1.2 Chapter Organization 2

Chapter 2 TEM Imaging of Core-Shell Nanowires 4

2.1 Growth Description 4

2.2 Planar TEM Imaging 6

2.3 Cross-sectional TEM Imaging 8

Chapter 3 Strain Simulation and Raman Spectra of Core-Shell Nanowires 15

3.1 Introduction and Background 15

3.1.1 Introduction to Strain 15

3.1.2 Raman Spectrum Measurement 16

3.2 Strain Simulation by Finite Element Method 18

3.3 Raman Spectra of Core-Shell Nanowires 19

3.4 Calculate Raman Modes Shift Using Lattice Dynamic Theory.....22

3.5 Simulation Results of Strain Distribution for Core-Shell Nanowire Hetertostructures and Calculation of Strain induced Raman Shift.....26

Chapter 4 Analysis of Core-Shell Nanowire Growth Result.....30

Chapter 5 Conclusion and Future Work.....33

Reference.....34

Vita.....41

List of Tables

Table 2.1: Core-shell Nanowire Growth Parameters 5

Table 2.2: Specifications of Core-shell Nanowire Growth Studied in This Thesis 6

Table 2.3: Surface Energy for Various Surfaces of Diamond Structure Crystals of Si and Ge.....13

Table 3.1: Lattice Constant and Cubic Elastic Stiffness of Si and Ge.....19

Table 3.2: Normalized Phonon Deformation Potentials for Si and Ge.....26

List of Figures

Figure 2.1: Schematic illustrating Ge−Si_xGe_{1-x} or Si−Si_xGe_{1-x} core−shell nanowire growth process 5

Figure 2.2: Planar TEM images of Ge−Si_xGe_{1-x} and Si−Si_xGe_{1-x} core−shell nanowires 8

Figure 2.3: Determination of the reciprocal lattice indices in FFTs using standard diffraction pattern.....8

Figure 2.4: Cross-sectional TEM image of a <110> oriented Si nanowire.....9

Figure 2.5: Schematics, HRTEM, FFT, STEM images of three different kinds of nanowires discussed in this thesis.....14

Figure 3.1: Raman spectra collected from individual Ge and Si nanowires 17

Figure 3.2: Raman spectrum of individual Ge−Si_xGe_{1-x} core-shell nanowire 20

Figure 3.3: Comparison of Raman spectra between <110> and <112> oriented Si−Si_xGe_{1-x} core-shell nanowires 22

Figure 3.4: Raman modes shift and intensity calculations for core regions of core-shell nanowires.....25

Figure 3.5: Strain distribution and strain-induced Raman mode shift of Ge−Si_xGe_{1-x} core-shell nanowire.....28

Figure 3.6: Strain distribution and strain-induced Raman mode shift of Si−Si_xGe_{1-x} core-shell nanowire.....29

Figure 4.1: Shell thickness difference between <110> and <112> oriented Si−Si_xGe_{1-x} core-shell nanowires are exaggerated at higher shell growth temperature 31

Figure 4.2: Cross-sectional TEM image of Si−Si_xGe_{1-x} core-shell nanowire with a very thin shell.....32

Chapter 1: Introduction

1.1 MOTIVATION AND THESIS HIGHLIGHT

One-dimensional semiconducting nanowires are attractive building blocks for nanoscale electronics, and photonic devices. Examples include nanowire field effect transistors [1-4] and solar cells [5]. Core-shell nanowire heterostructures have attracted attention because of one-dimensional carrier quantum confinement thanks to the radial band offset of various group IV or III-V compounds [6-10]. Lattice mismatch is inherent in core-shell nanowire heterostructures, and the induced strain will necessarily impact the band structure of semiconductors [11]. Because of their non-planar geometry, the elastic strain in core-shell nanowires depends not only on the lattice mismatch between the core and shell, but also on the nanowire diameter, shell thickness, and most interestingly on the shell morphology. While it is common to assume, and pedagogically easier to describe, a cylindrical shape for both core and shell, an epitaxial crystal (shell) grown on a non-planar substrate may not be fully conformal. Indeed, a fully cylindrical epitaxial shell growth on a nanowire core would be terminated by many high index planes, as opposed to a few energetically favorable low index facets. Consequently, it is important to accurately determine the shell morphology in epitaxial core-shell nanowires and its impact on the elastic strain, and correlate these findings with Raman spectra which probe the phonon energies in core-shell nanowires.

Cylindrical morphology for both core and shell have been considered for the purpose of strain calculations in group IV-based nanowires [12-14], and hexagonal

morphology examined for III-V compound-based nanowires [15, 16]. While group IV core-shell nanowires such as Ge−Si_xGe_{1-x} and Si−Si_xGe_{1-x} core-shell nanowires are attractive for MOSFET devices, their shell morphology and its impact on the properties of core-shell nanowires have not been systematically studied. In this study we conduct an experimental characterization of the shell morphology for both Ge−Si_xGe_{1-x} and Si−Si_xGe_{1-x} core-shell nanowires, calculate the elastic strain and optical phonon frequencies using a continuum elasticity model coupled with lattice dynamic theory, and compare the results with measured Raman spectra of individual nanowires. Both Ge−Si_xGe_{1-x} and Si−Si_xGe_{1-x} core-shell nanowires reveal cylindrical cores and hexagonal shells. Ge−Si_xGe_{1-x} core-shell nanowires grow along the <111> axis, with shell terminated by six {112} planes. The growth direction of Si−Si_xGe_{1-x} can be either <110> or <112>, with the <110> oriented nanowires bounded by two {100} and four {111} planes, and the <112> oriented nanowires bounded by two {111} and four {113} planes. The calculated and measured optical phonon frequencies in of the core regions are in good agreement.

1.2 CHAPTER ORGANIZATION:

Chapter 2 is devoted to transmission electron microscopy (TEM) imaging and analysis on Ge−Si_xGe_{1-x} as well as Si−Si_xGe_{1-x} core-shell nanowires. First the growth methodology is described. Planar TEM images will then be presented to show the single crystal nature of our nanowires, the epitaxial shell growth on the core, and will also serve to identify the growth direction. Cross-sectional TEM images reveal the morphology of the above mentioned core-shell nanowire heterostructures, with cylindrical core and hexagonal

shell. The distinct morphology between core and shell is attributed to the interplay between crystal growth and atom diffusion rate.

One main attribute of such heterostructure is the elastic strain associated with lattice mismatch between the core and shell, whose magnitude is determined by the dimension and core/shell morphology. The strain will shift the optical phonon frequencies and therefore have an impact on the Raman spectra for the core-shell nanowires. We address the two phenomena using finite element simulations, combined with Raman spectroscopy, for both Ge−Si_xGe_{1-x} and the two types of Si−Si_xGe_{1-x} core-shell nanowires.

Chapter 3 is dedicated to the simulation of strain distribution throughout the core-shell nanowire heterostructures, and the relevant Raman spectra. The simulated structure is based on the cross-sectional TEM imaging results. The simulation approach will be detailed and the results will be presented. Lattice dynamic theory is then applied to correlate strain with Raman mode shifts. The core Raman modes, calculated using the morphology determined from TEM images, demonstrate better agreement with experimental data, by comparison with those assuming a simplification of cylindrical co-axial structure. This emphasizes the significance of the morphology study in structural analysis on core-shell nanowires.

Chapter 4 is used to present, analyze and explain some interesting findings in the growth result, such as the shell growth rate dependence on the nanowire growth axis.

Chapter 5 serves to summarize this thesis and discuss future work.

Chapter 2: TEM Imaging of Core-Shell Nanowires[1]

2.1 GROWTH DESCRIPTION:

Figure 2.1 illustrates the growth of Ge−Si_xGe_{1-x} and Si−Si_xGe_{1-x} core-shell nanowires investigated in the study. The growth consists of a sequence of vapor-liquid-solid (VLS) core growth, followed by *in-situ* shell growth using ultra-high-vacuum chemical vapor deposition (CVD). An 8 Å thick Au film is evaporated onto a Si (111) substrate following the removal of native oxide using diluted hydrofluoric acid. The substrate is then transferred to a cold wall ultra-high-vacuum CVD chamber, and annealed in a H_2 ambient at 370 °C, which leads to the formation of Au-Si eutectic alloy particles of around 20 nm in diameter that serve as catalysts for the VLS growth. The Ge nanowire cores are grown at a temperature of 270 °C and pressure of 2.5 Torr using GeH_4 (20% diluted in He) as precursor, while the Si nanowire cores are grown at 460 °C and 10 Torr using SiH_4 (100%) as precursor. The epitaxial Si_xGe_{1-x} shell growth is then performed *in-situ* at a temperature of 390 °C, 40 mTorr pressure, using a mixture of GeH_4 and SiH_4, with flows detailed in Table 2.1. Table 2.2 summarizes the growth conditions for the different samples examined in this thesis. Bare Ge and Si nanowires have also been grown to serve as baselines to understand core morphology and extract unstrained optical phonon frequencies.

[1] Chapter 2 is based on a prior publication, F. Wen, D.C. Dillen, K. Kim, E. Tutuc, Journal of Applied Physics 121 (23), 234302. F.W. performed the nanowire growth, TEM, Raman measurement and calculations, D.C.D. and K.K. help with facility training. F.W. and E.T. analyzed the data and co-wrote the paper.

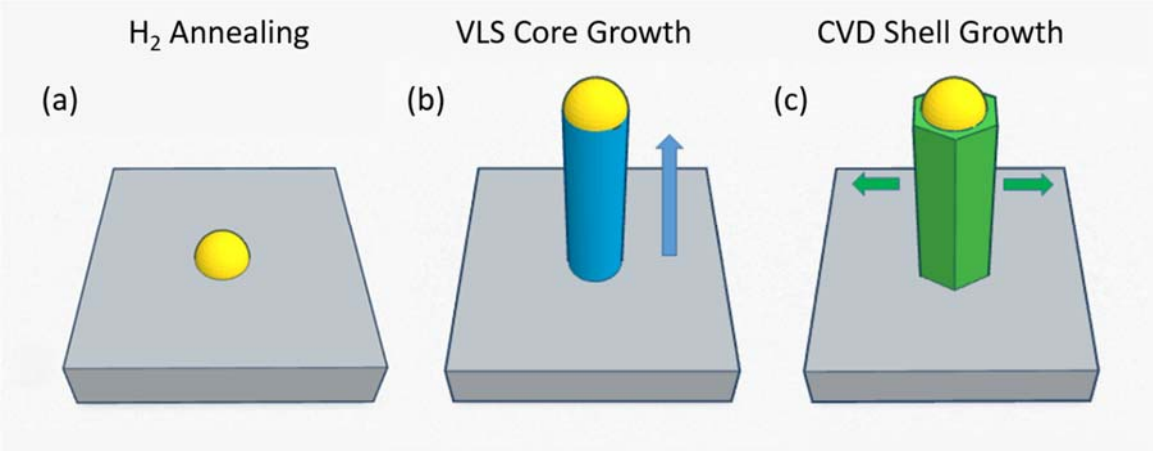

Figure 2.1 Schematic illustrating Ge−Si_xGe_{1-x} or Si−Si_xGe_{1-x} core−shell nanowire growth process. (a) Hydrogen annealing. (b) Vapor−liquid−solid core growth. (c) Epitaxial shell growth. Arrows represent the growth direction in each growth regime.

Table 2.1. Core-shell Nanowire Growth Parameters

Core-shell nanowire type	GeH_4/SiH_4 flow during core growth (s.c.c.m.)	GeH_4/SiH_4 flow during shell growth (s.c.c.m.)
Ge−Si_xGe_{1-x}	50/0	10/50
Si−Si_xGe_{1-x}	0/100	10/50

Table 2.2. Specifications of Core-shell Nanowire Growth Studied in This Thesis

Sample Name	Growth Type	Shell Growth Temp.	Shell Si Content[1]	t_{sh} {112}	t_{sh} {100}	t_{sh} {111}[2]	t_{sh} {111}[3]	t_{sh} {113}
A	Ge−Si_xGe_{1-x}	385 °C	57%	4.5 nm	N/A	N/A	N/A	N/A
B	Si−Si_xGe_{1-x}	390 °C	65%	N/A	2.9 nm	3.0 nm	3.3 nm	5.0 nm
C	Si−Si_xGe_{1-x}	420 °C	68%	N/A	3.3 nm	3.4 nm	4.8 nm	7.8 nm
D	Si−Si_xGe_{1-x}	450 °C	79%	N/A	3.0 nm	3.1 nm	5.6 nm	9.5 nm

1: The method to extract the shell Si content will be discussed in Chapter 3.5.

2: This column represents the {111} facets shell thickness for the Si−Si_xGe_{1-x} core-shell nanowires oriented along the <110> direction.

3: This column represents the {111} facets shell thickness for the Si−Si_xGe_{1-x} core-shell nanowires oriented along the <112> direction.

2.2 PLANAR TEM IMAGING:

We have performed plane view TEM imaging on the nanowires after dispersing them on carbon lacey copper grid. The growth direction of Ge−Si_xGe_{1-x} core-shell nanowires is along <111> crystal axis, and that of the Si−Si_xGe_{1-x} core-shell nanowires can be either <110> or <112> crystal axes. We have experimentally found that the <112> oriented nanowires can be eliminated if the growth temperature is reduced from 460 °C to

420 °C, and the SiH_4 precursor partial pressure is increased from 5 Torr to 10 Torr during the Si core growth. Figure 2.2(a-c) illustrate planar TEM images of a <111> oriented Ge−Si_xGe_{1-x} core-shell nanowire, <110> and <112> oriented Si−Si_xGe_{1-x} core-shell nanowires, respectively. We note that the shell is grown epitaxially on core, with smooth sidewalls. The insets are the corresponding fast Fourier transforms (FFTs) of the TEM images. The orientation can be determined by investigating the diffraction pattern or the FFT. As shown in the insets, the axial orientations of the nanowires are mapped from the TEM images to their FFTs directly, which are marked along the arrows. If the arrow points from one reflection (reciprocal lattice) to its symmetric points about the center in the FFT, then the index of that reflection reveals the axial orientation of the nanowire. E.g. in the inset of Figure 2.2(a), the arrow points from $(\bar{1}\bar{1}\bar{1})$ to (111) reflection, therefore the axial orientation of the nanowire is [111]. Figure 2.3(a-c) presents the approach to label the reciprocal lattice indices for the three types of nanowires, respectively. The FFTs are compared with standard diffraction patterns of cubic Si/Ge assuming the electron beam along a certain zone axis, the reciprocal lattice indices are then revealed by overlapping the diffraction spots in the FFTs with those in the standard patterns. The reciprocal lattice constants can help identify the crystal plane indices quickly, which can be directly measured using the distance between individual reflection spot with the direct beam spot in the center of FFTs. It is noteworthy that in Fig. 2.3(c), the FFT of <112> oriented Si−Si_xGe_{1-x} core-shell nanowire shows 1/3{422} reflections along [111] zone axis, which are kinetically forbidden for face-centered cubic crystal like Si and Ge. Their appearance is attributed to {111} stacking faults and interpenetrating twins [17].

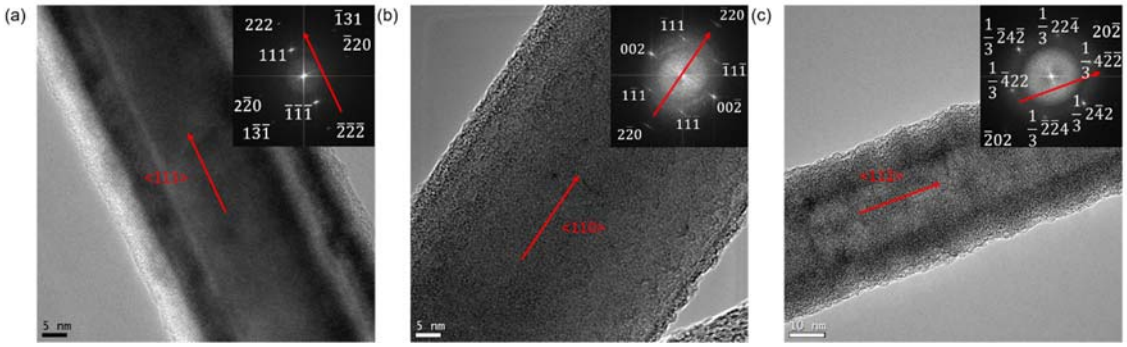

Figure 2.2 Planar TEM images of Ge−Si_xGe_{1-x} and Si−Si_xGe_{1-x} core−shell nanowires. (a) <111> oriented Ge−Si_xGe_{1-x} core-shell nanowire. (b) <110> oriented Si−Si_xGe_{1-x} core-shell nanowire. (c) <112> oriented Si−Si_xGe_{1-x} core-shell nanowire. The insets are the associated FFTs of the TEM images. Arrows indicate the growth directions in each panel.

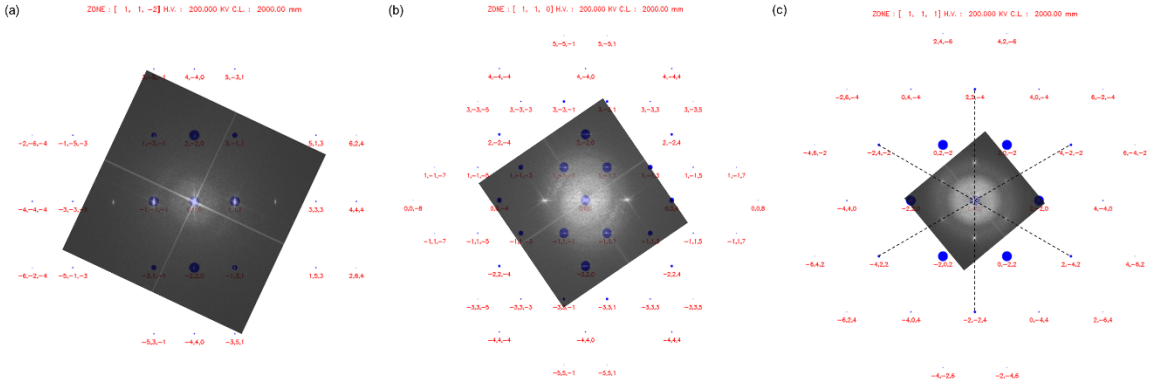

Figure 2.3 Determination of the reciprocal lattice indices in FFTs as in Fig. 2.2 by overlapping FFTs and the standard diffraction patterns of Si/Ge. (a) <111> oriented Ge−Si_xGe_{1-x} core-shell nanowire, assuming the zone axis along $[11\bar{2}]$. (b) <110> oriented Si−Si_xGe_{1-x} core-shell nanowire, assuming the zone axis along [110]. (c) <112> oriented Si−Si_xGe_{1-x} core-shell nanowire, assuming the zone axis along [111].

2.2 CROSS-SECTIONAL TEM IMAGING:

Planar TEM cannot provide information about the core and shell morphology. To address this problem, we employ cross-sectional transmission electron microscopy to probe the crystal structure and shell morphology of both Ge−Si_xGe_{1-x} and Si−Si_xGe_{1-x} core-shell nanowires. Cross-sectional TEM sample preparation method is detailed as follows: A

solution of nanowires, prepared by sonicating the growth wafer in ethanol, is dispersed onto a patterned Si substrate with 285 nm SiO_2 grown by thermal oxidation. An Al_2O_3 film is subsequently deposited by atomic layer deposition. The amorphous SiO_2 and Al_2O_3 oxide films provide a sharp contrast and well-defined boundaries with respect to the single crystal nanowire cross-sections. A patterned TaN film is used as a protective layer and alignment mark for dicing, and focus ion beam (FIB) milling. The resulting nanowire cross-section samples are usually 50 nm to 100 nm in thickness. Bare Si nanowires are also processed to identify the core morphology. Figure 2.4 presents a cross-sectional TEM image of a <110> oriented Si nanowire, which clearly exhibits a cylindrical shape.

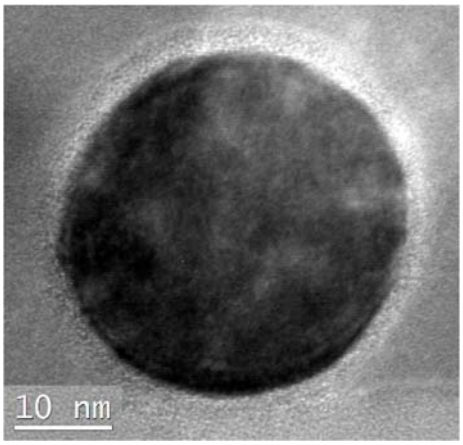

Figure 2.4 Cross-sectional TEM image of a <110> oriented Si nanowire.

Figure 2.5 presents the results of cross-sectional TEM imaging on Ge−Si_xGe_{1-x} [panels (a-d)] and Si−Si_xGe_{1-x} [panels (e-l)] core-shell nanowires, for growth A and B in Table 2, respectively. Figure 2.5(a) shows a schematic of a Ge−Si_xGe_{1-x} core-shell nanowire, constructed based on the high resolution transmission electron microscopy (HRTEM) data of Fig. 2.5(b), their FFT of Fig. 2.5(c), as well as the dark field scanning

transmission electron microscopy (STEM) data of Fig. 2.5(d). The data of Fig. 2.5(b-d) reveals a cylindrical Ge nanowire core, and a faceted epitaxial shell with a regular hexagonal cross section. Examination of the FFT data of Fig. 2.5(c) reveals spots associated with the {224} and {220} planes. Comparing these data with standard diffraction patterns allows us to identify the <111> crystal axis as the nanowire growth direction. Because the orientation of Fig. 2.5(b) and 2.5(c) data are identical we can translate the diffraction spots to plane indices in Fig. 2.5(b), and unambiguously identify the shell facets as the {112} planes. We note that TEM data acquired for multiple Ge−Si_xGe_{1-x} core-shell nanowire growths are all consistent with Fig. 2.5(b-d).

For Si−Si_xGe_{1-x} core-shell nanowire heterostructures however, the TEM analysis of multiple samples reveals cylindrical Si cores with two distinct shell morphologies, which we label in the following as type I and type II. Figure 2.5(e) represents the schematic of type I Si−Si_xGe_{1-x} core-shell nanowires, constructed based on the HRTEM data of Fig. 2.5(f), the corresponding FFT data of Fig. 2.5(g), as well as STEM data of Fig. 2.5(h). Figure. 2.5(i) represent the schematic of type II Si−Si_xGe_{1-x} core-shell nanowires, constructed based on the HRTEM data of Fig. 2.5(j), the corresponding FFT data of Fig. 2.5(k), as well as STEM data of Fig. 2.45(l). By comparison to the type I shell morphology, type II samples show a hexagonal shell elongated along one direction, with a non-uniform thickness. The FFT data of Fig. 2.5(f) and 2.5(j) and reveal spots associated with the {200}, {220}, {113} and {111} planes for type I, and {111}, {220}, {042} and {113} planes for type II Si−Si_xGe_{1-x} core-shell nanowires, respectively. For type I nanowires the angle between two equivalent (inequivalent) facets is 110° (125°), while for type II nanowires

equivalent (inequivalent) facets form a 117.3° (121.4°) angle. A comparison of these values with the angles between different crystal planes allows us to identify two {100} and four {111} planes as the facets of type I nanowires, corresponding to a <110> growth axis, and also two {111} and four {113} planes as the shell facets of type II nanowires, corresponding to a <112> growth direction. The data of Fig. 2.5(e-l), and the presence of two distinct shell morphologies have been verified in multiple samples and in different growths.

Particularly noteworthy, the contrast between the cylindrical core and the hexagonal shell morphologies can be related to the interplay between growth rate and surface diffusion during the VLS and CVD growth modes. Because the Au-catalyzed core VLS growth has a much higher precursor partial pressure, and thus growth rate compared to the un-catalyzed shell CVD growth, the ratio of diffusion to deposition rate for adatoms during core growth is significantly lower compared to the shell growth. The surface diffusion of adatoms during shell growth allows it to reach a morphology dictated by surface energy consideration. For diamond cubic crystals like Si and Ge, the surface should be terminated with low-index planes that minimize the surface energy. If the surface diffusion is low compared to growth rate during shell growth, the shell growth will be conformal, hence cylindrical. The above argument applies not only to the shell growth, but also to the nanowire core growth. Indeed, <111> oriented Si nanowires grown at lower (below 100 mTorr) SiH_4 partial pressures and elevated (above 500 °C) temperatures compared to our study, hence in a regime where the surface diffusion is dominant, have

been shown to possess six {112} facets [18-20], consistent with theoretical calculations [21].

Energetic considerations (see Table 2.3 for Si/Ge surface energy) indicate that Si nanowires grown along <110> crystal axis should be bound by two {100} and four {111} planes [22], similar to <110> Si−Si_xGe_{1-x} core-shell nanowire morphology of Fig. 2.5(e). Experimental observations of Si nanowire growth by the VLS mechanism along the <112> direction are less common, and appear to be associated with the presence of hexagonal phases [23]. An early study of Si micro-rods [24] oriented along the <112> crystal axis shows {111} and {113} facets, similar to the <112> nanowire morphology of Fig. 2.5(i). This combination of facets cannot be solely explained by surface energy considerations because {113} planes are expected to have much higher surface energy compared to low-index {100}, {110} and {111} planes, even after taking surface reconstruction into account [25].

Table 2.3. Surface Energy for Various Surfaces of Diamond Structure Crystals of Si and Ge [21]

Surface Orientation	Si (ergs/cm^2)	Ge (ergs/cm^2)
{100}	1879.82	1657.18
{110}	1535.88	1412.78
{111}	1254.24	1153.72
{112}	1330.28	1223.66
{113}	2921.98	2600.99

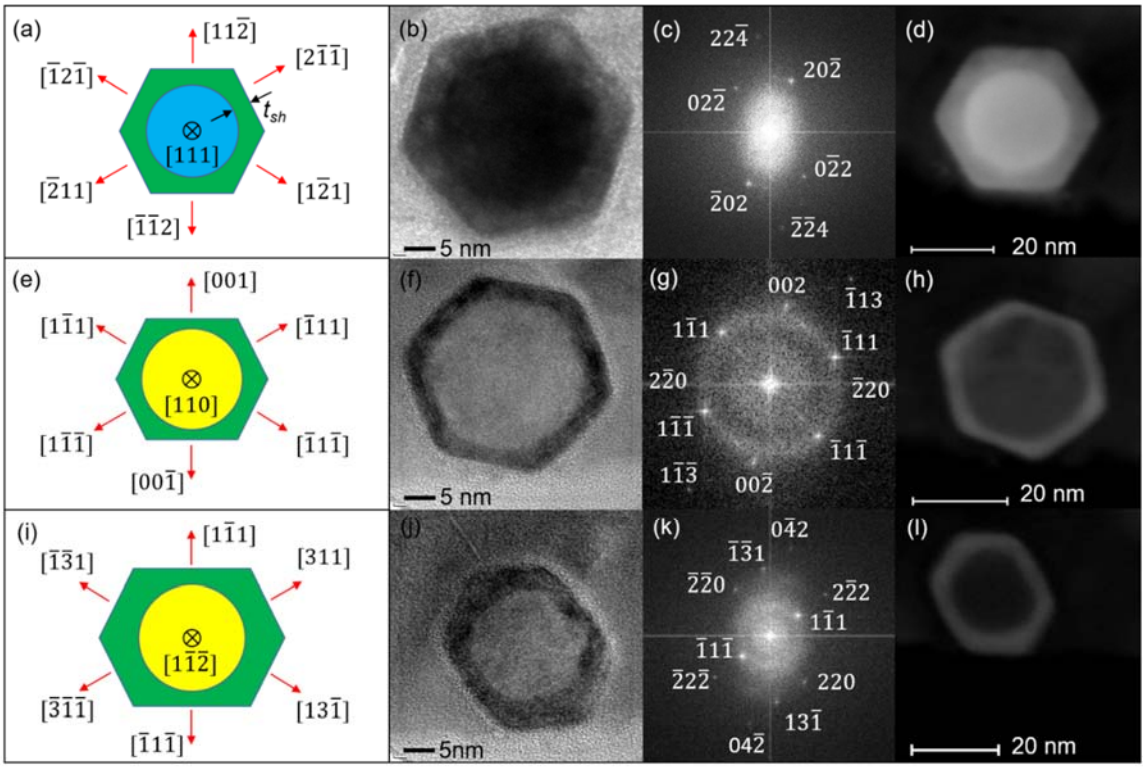

Figure 2.5 Schematics, HRTEM, FFT, STEM images of three different kinds of nanowires discussed in this thesis. The HRTEM images and their FFTs are identical in orientation, enabling a direct correspondence between FFTs to plane indices in real space images. (a) Ge−Si_xGe_{1-x} nanowire with the growth direction along the <111> axis, showing a cylindrical Ge core, and hexagonal Si_xGe_{1-x} shell with six {112} facets. (b-d) Cross-sectional HRTEM, FFT and STEM of a Ge−Si_xGe_{1-x} nanowire. (e) Type I Si−Si_xGe_{1-x} nanowire with the growth direction along the <110> axis, showing a cylindrical Si core and hexagonal Si_xGe_{1-x} shell with two {100} and four {111} facets. (f-h) Cross-sectional HRTEM, FFT and STEM of a <110> oriented Si−Si_xGe_{1-x} nanowire. (i) Type II Si−Si_xGe_{1-x} nanowire with the growth direction along the <112> axis, showing a cylindrical Si core and hexagonal Si_xGe_{1-x} shell with two {111} and four {113} facets. (j-l) Cross-sectional HRTEM, FFT and STEM of a <112> oriented Si−Si_xGe_{1-x} nanowire.

Chapter 3: Strain Simulation and Raman Spectra of Core-Shell Nanowires[2]

3.1 INTRODUCTION AND BACKGROUND:

3.1.1 INTRODUCTION TO STRAIN:

Elastic strain is defined as the measure of deformation representing the displacement between particles in the body relative to a reference length. Displacement is a vector field defining the change in position of a given point between the strained and unstrained cases. The displacement, $\boldsymbol{u}$, and the strain tensor are linked through the following equation in Cartesian coordinates:

$$\varepsilon_{ij} = \frac{1}{2}\left(\frac{du_i}{dx_j} + \frac{du_j}{dx_i}\right) \tag{3.1}$$

In 3-dimensional case, strain can be expressed as a second rank tensor:

$$\varepsilon_{ij} = \begin{bmatrix} \varepsilon_{xx} & \varepsilon_{xy} & \varepsilon_{xz} \\ \varepsilon_{yx} & \varepsilon_{yy} & \varepsilon_{yz} \\ \varepsilon_{zx} & \varepsilon_{zy} & \varepsilon_{zz} \end{bmatrix} \tag{3.2}$$

The indices above are the same as those of the stress, they correspond to the direction of force and the surface normal on which it is acting, e.g. ε_{yx} indicates a deformation in the y direction of a surface whose normal is along x direction. Terms along the main diagonal of Eq. (3.1) are normal components of strain representing tension or

[2] Chapter 3 is based on a prior publication, F. Wen, D.C. Dillen, K. Kim, E. Tutuc, Journal of Applied Physics 121 (23), 234302. F.W. performed the nanowire growth, TEM, Raman measurement and calculations, D.C.D. and K.K. help with facility training. F.W. and E.T. analyzed the data and co-wrote the paper.

compression along certain direction. The sign of strain indicates the type of deformation present: a negative value designates a compressive strain, while positive strain is a tensile one. Off-diagonal terms are shear components, resulting in shear deformation. The requirement of no rigid body translations or rotations forces off-diagonal shear terms to be symmetric, e.g. $\varepsilon_{yx} = \varepsilon_{xy}$. Hence the 9-component strain tensor can be reduced to 6 terms. For cubic crystal like Si and Ge, stress can be directly related to strain through Hooke's Law:

$$\begin{bmatrix} \varepsilon_{xx} \\ \varepsilon_{yy} \\ \varepsilon_{zz} \\ 2\varepsilon_{yz} \\ 2\varepsilon_{zx} \\ 2\varepsilon_{xy} \end{bmatrix} = \begin{bmatrix} C_{11} & C_{12} & C_{12} & 0 & 0 & 0 \\ C_{12} & C_{11} & C_{12} & 0 & 0 & 0 \\ C_{12} & C_{12} & C_{11} & 0 & 0 & 0 \\ 0 & 0 & 0 & C_{44} & 0 & 0 \\ 0 & 0 & 0 & 0 & C_{44} & 0 \\ 0 & 0 & 0 & 0 & 0 & C_{44} \end{bmatrix} \begin{bmatrix} \sigma_{xx} \\ \sigma_{yy} \\ \sigma_{zz} \\ \sigma_{yz} \\ \sigma_{zx} \\ \sigma_{xy} \end{bmatrix} \tag{3.3}$$

where C_{ij} are the material's elastic stiffness constants, forming a second rank tensor of 36 terms. The cubic crystal symmetry reduces the required number of terms to three: C_{11}, C_{12} and C_{44}. Stress is expressed in units of Pascals and can be thought of as pressure in a material due to an applied force. Similar to strain tensor, stress tensor σ_{ij} is also symmetric and reduced to 6 components.

3.1.2 RAMAN SPECTRUM MEASUREMENT:

Raman measurements were conducted using a Renishaw InVia μ-Raman spectrometer with backscattering geometry, 532 nm incident laser with around 1μm focused spot size and 13kW·cm^{-2} power density, and 100× objective lens. Raman measurements were first done on bare Ge and Si nanowires to provide a baseline for the

strain-induced shift of the Ge-Ge and Si-Si Raman modes in core-shell samples. We have evaporated 20 nm Ti and 60 nm Au onto the substrate before dispersing nanowires to eliminate Raman signals originating from the substrate that can overlap with those from the nanowires. We find the unstrained Ge-Ge and Si-Si mode frequencies are 300.5 cm^{-1} and 520.6 cm^{-1} respectively for the bare Ge and Si nanowires in our system, independent on diameter. A second kind of Si nanowire Raman spectrum with two Raman modes is also observed, with the nominal Si-Si mode slightly red-shifted from 520.6 cm^{-1} and one additional Si-Si mode at around 495 cm^{-1}. The spectra of the three mentioned kinds of nanowires is shown in Figure 3.1.

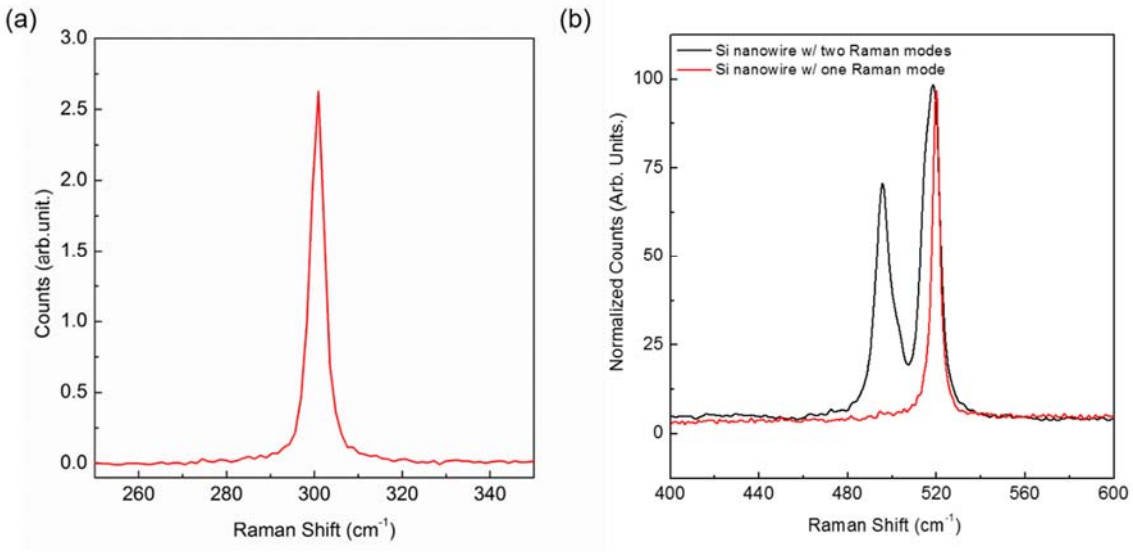

Figure 3.1 Raman spectra collected from individual Ge and Si nanowires. (a) Raman spectrum of Ge nanowire. (b) Raman spectra of two kinds of Si nanowires.

3.2 STRAIN CALCULATIONS USING FINITE ELEMENT METHOD:

We calculate the elastic strain using a finite element modelling package (Abaqus®, Dassault Systemes). The simulated structure is a three dimensional rod, with a sufficiently large length to approximate an infinite nanowire. The shell thickness (t_{sh}) is defined for each facet along the perpendicular from the core center to the facet plane [(see Fig. 2.5(a)]. The shell thicknesses and crystal orientations are based on TEM results of growth C in Table 2.2. For the Ge−Si_xGe_{1-x} core-shell nanowires examined here t_{sh} = 4.5 nm. For <110> oriented Si−Si_xGe_{1-x} core-shell nanowires t_{sh} = 3.3 nm and t_{sh} = 3.4 nm for the {100} and {111} facets, respectively, while for <112> oriented Si−Si_xGe_{1-x} core-shell nanowires t_{sh} = 4.8 nm and t_{sh} = 7.8 nm for the {111} and {113} facets, respectively. Lattice mismatch between core and shell is simulated by giving shell a thermal expansion coefficient α_s and heating the heterostructure from an initial temperature (T_i) to a final temperature (T_f). The values are chosen to satisfy Equation (3.4), and actual values are unimportant.

$$\alpha_s(T_f - T_i) = \frac{l_s - l_c}{l_c} \tag{3.4}$$

where l_s and l_c are lattice constants of shell and core respectively. To extract meaningful strain tensor values, the simulated shell strain tensor normal components need a subtraction of the isotropic hydrostatic strain due to thermal expansion, and all the shear components need to be divided by 2 as Abaqus uses engineering strain. The elastic stiffness matrix of Table 3.1 is used to determine the linear response to stress, an approach which captures the elastic anisotropy of each material.

Table 3.1. Lattice Constant and Cubic Elastic Stiffness of Si and Ge [26, 27]

Material	Lattice Parameter (Å)	C_{11} (GPa)	C_{12} (GPa)	C_{44} (GPa)
Si	5.431	165.8	63.9	79.6
Ge	5.658	128.5	48.3	66.8

Lattice constants and elastic stiffness of Si_xGe_{1-x} alloy are calculated as linear interpolation between those of Si and Ge.

3.3 RAMAN SPECTRA OF CORE-SHELL NANOWIRES:

Figure 3.2 reveals the Raman spectrum of a Ge−Si_xGe_{1-x} core-shell nanowire. Four Raman modes are observed, including the Ge-Ge Raman modes of both core and shell, the Si-Ge and Si-Si Raman modes of the Si_xGe_{1-x} shell. The core Ge-Ge Raman mode shows a blue shift from the bulk value due to compressive strain. Two Si-Ge Raman modes are observed for the Si_xGe_{1-x} shell, due to localized Si-Si motion in the neighborhood of different number of Ge atoms in the alloy [28].

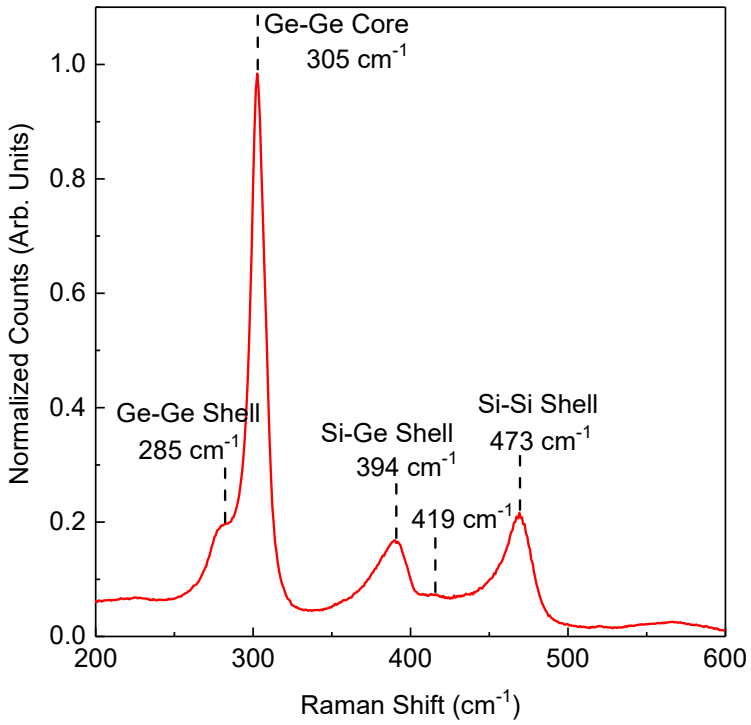

Figure 3.2 Raman spectrum of individual Ge−Si_xGe_{1-x} core-shell nanowire. The peaks associated with individual Raman mode are marked with a vertical dashed line.

We now turn to the Raman signature of the two types of Si−Si_xGe_{1-x} core-shell nanowires. Figure 3.3(a) and 3.3(b) show examples of Raman spectra for the two types of Si−Si_xGe_{1-x} core-shell heterostructures discussed in Fig. 2.5 for growth C in Table 2.2. Figure 3.3(a) shows an example of Raman spectrum revealing two peaks at 515 cm^{-1} and 504 cm^{-1}, which we associate with the Si-Si mode from the core and shell, respectively. The core Si-Si mode is red shifted with respect to the unstrained Si-Si Raman mode of 520.6 cm^{-1}, indicating a tensile strain. Also visible in Fig. 3.3(a) data are the Ge-Ge mode at 292 cm^{-1}, originating from the shell, and two peaks at 409 cm^{-1} and 434 cm^{-1}, associated with the Si-Ge modes of the shell. Figure 3.3(a) inset shows a cross-sectional TEM micrograph of the *same* nanowire the main panel data was acquired from, which reveals

the heterostructure is type I, oriented along <110>. Figure 3.3(b) shows a Raman spectrum similar to Fig. 3.3(a) data, but with a third Si-Si peak at 487 cm^{-1}. Also noteworthy, Fig. 3.3(b) data shows that the core Si-Si mode has a larger red shift by comparison to the unstrained Si-Si Raman mode than Fig. 3.3(a) data. The inset of Fig. 3.3(b) shows a cross-sectional TEM micrograph of the *same* nanowire, revealing a type II heterostructure, oriented along <112>. We have verified the above correlation between absence (presence) of the third Si-Si peak in Raman spectra, with the type I (II) heterostructure via cross-sectional TEM in multiple nanowire samples. This result is in agreement with previous studies [23, 29] correlating the growth direction and Raman spectra in bare Si nanowire, which show that Si nanowires oriented along the <112> direction exhibit an additional Si-Si peak, associated with hexagonal phases. The correlation between Raman signature and growth direction described in Figure 3.3 is further substantiated by Raman spectra collected from individual Si nanowire, which exhibit either a single peak at 520.6 cm^{-1}, or two peaks at 518.5-520 cm^{-1} and 495-497 cm^{-1}, as shown in Fig. 3.1(b). Our nanowires do not exhibit kinking [30], and the Raman spectra collected at different positions along the nanowire are very similar, indicating the crystal structure and growth direction stem from the nucleation phase.

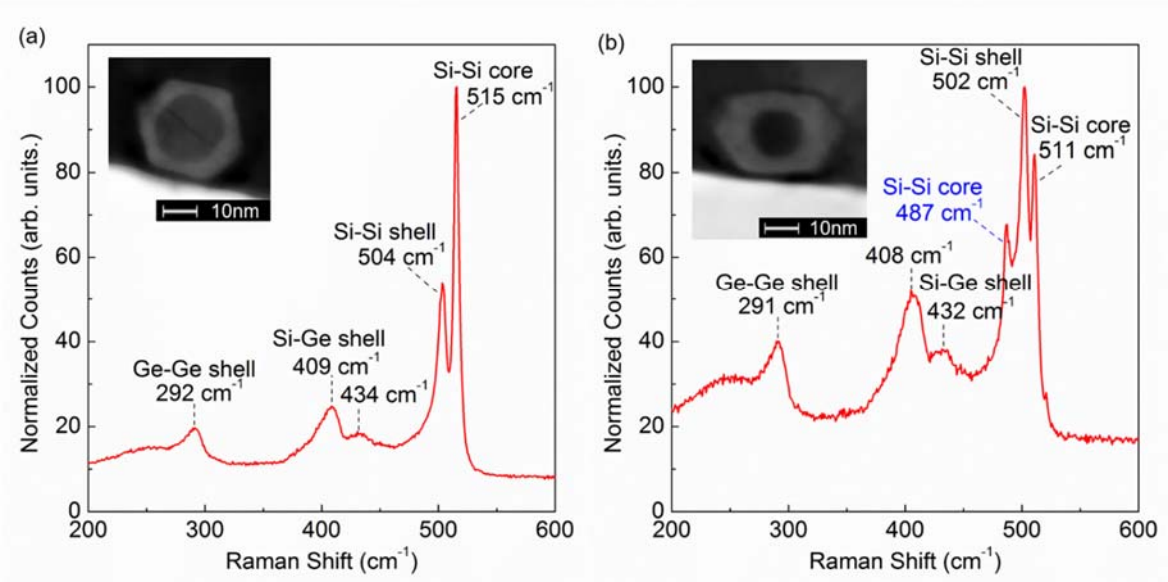

Figure 3.3 Comparison of Raman spectra between <110> and <112> oriented Si−Si_xGe_{1-x} core-shell nanowires. (a) Raman spectrum of a <110> oriented Si−Si_xGe_{1-x} core-shell nanowire with two Si-Si Raman modes. Inset: cross-sectional TEM micrograph of the same nanowire as in main panel. (b) Raman spectrum of a <112> oriented Si−Si_xGe_{1-x} core-shell nanowire with three Si-Si Raman modes. An additional Si-Si core mode is observed. The thicker shell leads to higher intensity of the Si-Si, Ge-Ge, and Si-Ge shell modes. Inset: cross-sectional TEM micrograph of the same nanowire.

3.4 CALCULATE RAMAN MODES SHIFT USING LATTICE DYNAMIC THEORY:

The impact of elastic strain on the optical phonon frequencies is calculated using lattice dynamic theory. Generally, the elastic strain shifts and splits the triply degenerate optical phonon modes at zone center in a cubic crystal. The strain-induced shift of each optical phonon branch, and the corresponding Raman mode can be calculated by applying the secular equation of lattice dynamic theory [31, 32]:

$$\begin{vmatrix} p\varepsilon_{xx} + q(\varepsilon_{yy} + \varepsilon_{zz}) - \lambda & 2r\varepsilon_{xy} & 2r\varepsilon_{xz} \\ 2r\varepsilon_{xy} & p\varepsilon_{yy} + q(\varepsilon_{xx} + \varepsilon_{zz}) - \lambda & 2r\varepsilon_{yz} \\ 2r\varepsilon_{xz} & 2r\varepsilon_{yz} & p\varepsilon_{zz} + q(\varepsilon_{xx} + \varepsilon_{yy}) - \lambda \end{vmatrix} = 0, \tag{3.5}$$

where ε_{ij} are the strain tensor components and p, q, and r are the material's phonon deformation potential values, given in Table 3.2. The strain tensor components are referenced to the crystallographic axes, $\boldsymbol{u_1}$ = [100], $\boldsymbol{u_2}$ = [010], $\boldsymbol{u_3}$ = [001]. The eigenvalues $\lambda_i = \omega_i^2 - \omega_{i0}^2$ describe the strain-induced shift of mode i, where ω_{i0} is the frequency for zero strain. The eigenvectors describe the associated strained phonon wave vectors. The intensity of Raman mode i can thus be computed as follows [14, 33]:

$$I(i) \propto |\boldsymbol{E}_{inc}^T \cdot R'(i) \cdot \boldsymbol{E}_{scat}|^2 \tag{3.6}$$

where R'(i) is the Raman tensor for mode i, expressed in the following equation (3.7):

$$R'(i) = \sum_{j=1}^{3} (\boldsymbol{u_j} \cdot \boldsymbol{u_i'}) \cdot R(j) \tag{3.7}$$

where $\boldsymbol{u_i'}$ is the eigenvector corresponding to eigenvalue λ_i, $R(j)$ are Raman tensors for unstrained modes with $\mathbf{u_1}$, $\mathbf{u_2}$ and $\mathbf{u_3}$ as wave vectors, as shown in the following forms [34]:

$$R(1) = \begin{bmatrix} 0 & 0 & 0 \\ 0 & 0 & 1 \\ 0 & 1 & 0 \end{bmatrix}, \; R(2) = \begin{bmatrix} 0 & 0 & 1 \\ 0 & 0 & 0 \\ 1 & 0 & 0 \end{bmatrix}, \; R(3) = \begin{bmatrix} 0 & 1 & 0 \\ 1 & 0 & 0 \\ 0 & 0 & 0 \end{bmatrix} \tag{3.8}$$

To compare the relative intensity of the calculated Raman modes, the incident ($\boldsymbol{E}_{inc}$) and scattered ($\boldsymbol{E}_{scat}$) light polarization are assumed parallel to the nanowire axis. This assumption is theoretically justified by an "antenna effect" [35, 36], and experimentally

verified by a $\cos^2\theta$ dependence of the scattered beam intensity if the incident light polarization is aligned at an angle θ with respect to the nanowire main axis. As such we will assume $\boldsymbol{E}_{inc}$ || [111] for Ge−Si_xGe_{1-x} core-shell nanowire and $\boldsymbol{E}_{inc}$ || [110] or [112] for Si−Si_xGe_{1-x} core-shell nanowire. We have also experimentally verified $\boldsymbol{E}_{scat}$ to be parallel to $\boldsymbol{E}_{inc}$ by polarizing the scattered light.

Although the solution of the secular equation predicts three non-degenerate core Ge-Ge or Si-Si Raman modes, using Eq. (3.6) we find only one Ge-Ge or Si-Si core mode with significant intensity for all three types of core-shell nanowires discussed in this study, as shown in Figure 3.4. Figure 3.4(a-r) show examples of three calculated Raman modes and their intensity for <110>, <112> oriented Si−Si_xGe_{1-x} and <111> oriented Ge−Si_xGe_{1-x} core-shell nanowire, respectively, using the strain simulated as described in Chapter 3.2.

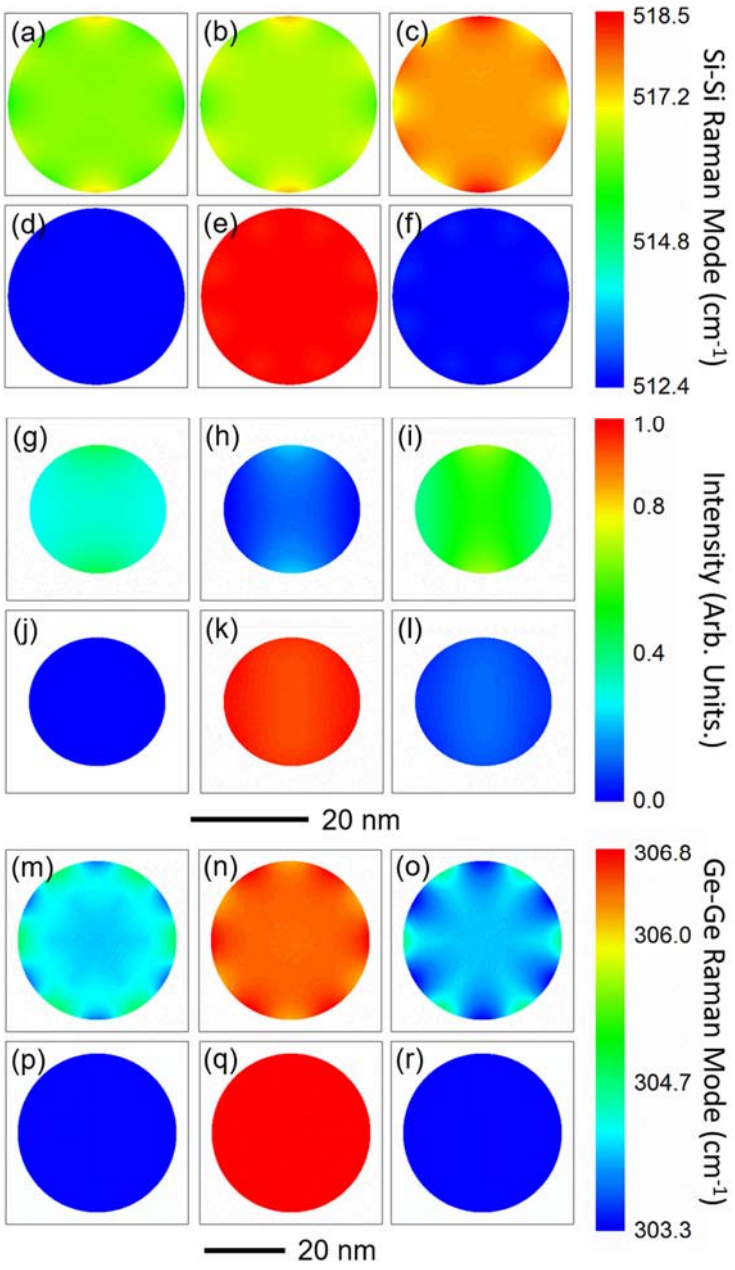

Figure 3.4 Raman modes shift and intensity calculations for core regions of core-shell nanowires. (a-c) Three Si-Si Raman modes in the core region of <110> oriented Si−Si_xGe_{1-x} core-shell nanowire and (d-f) the associated intensity. (g-i) Three Si-Si Raman modes in the core region of <112> oriented Si−Si_xGe_{1-x} core-shell nanowire and (j-l) the associated intensity. (m-o) Three Ge-Ge Raman modes in the core region of <111> oriented Ge−Si_xGe_{1-x} core-shell nanowires and (p-r) the associated intensity. Only one core Raman mode is active (with non-zero intensity) in each kind of nanowire. The upper dimension scale bar is for panel (a-l), while the lower dimension scale bar is for panel (m-r).

Table 3.2 Normalized Phonon Deformation Potentials for Si and Ge:

Material	p/ω_0^2	q/ω_0^2	r/ω_0^2
Si	-1.84[37]	-2.35[37]	-0.71[38]
Ge	-1.66[37]	-2.19[37]	-1.11[39]

3.5 SIMULATION RESULTS OF STRAIN DISTRIBUTION FOR CORE-SHELL NANOWIRE HETEROSTRUCTURE AND CALCULATION OF STRAIN INDUCED RAMAN SHIFT:

Figure 3.5 presents results for Ge−Si_xGe_{1-x} core-shell nanowires growth A, including diameter dependence of calculated and experimentally obtained core Ge-Ge Raman modes [Fig. 3.5(a)], along with two-dimensional contour plots of the strain distribution [Figs. 3.5(b) and 3.5(c)]. In Figure 3.5(a) we show the calculated Ge-Ge mode Raman shift as a function of nanowire diameter (d) for a Ge-Si_xGe_{1-x} core-shell nanowire heterostructures with t_{sh} = 4.5 nm, determined from cross-sectional TEM results. The Si:Ge shell content value, x = 0.57 is determined from the relative intensities of the Si-Si, Si-Ge, and Ge-Ge shell Raman modes in an individual Raman spectrum [40, 41].

We can extract the Ge shell content using the relative intensities of the Si-Si and Si-Ge Raman modes, or that of the Ge-Ge and Si-Ge Raman modes:

$$\frac{I(Si\text{-}Si)}{I(Si\text{-}Ge)} = \frac{A(1-x)}{2x} \qquad (3.9)$$

$$\frac{I(Ge\text{-}Ge)}{I(Si\text{-}Ge)} = \frac{Bx}{2(1-x)} \qquad (3.10)$$

where A and B are constants, whose values used are 1.85 and 3.2 respectively [40], *x* is the Ge content in the $Si_{1-x}Ge_x$ alloy.

A comparison between the calculated Raman shift for hexagonal and cylindrical cross-sections, assuming identical shell areas, shows very similar results, within the experimental error. For both cases, as the ratio of shell over core volume decreases with the nanowire diameter, the strain in the core and the strain-induced shift of the Ge-Ge Raman core mode are reduced. Altogether, Fig. 3.5 data indicate that while small differences exist between the strain, and corresponding Raman shift for cylindrical and hexagonal shell morphologies, the assumption of a cylindrical shell, perhaps more pedagogical is also a very good approximation to calculate the strain and corresponding Raman shift.

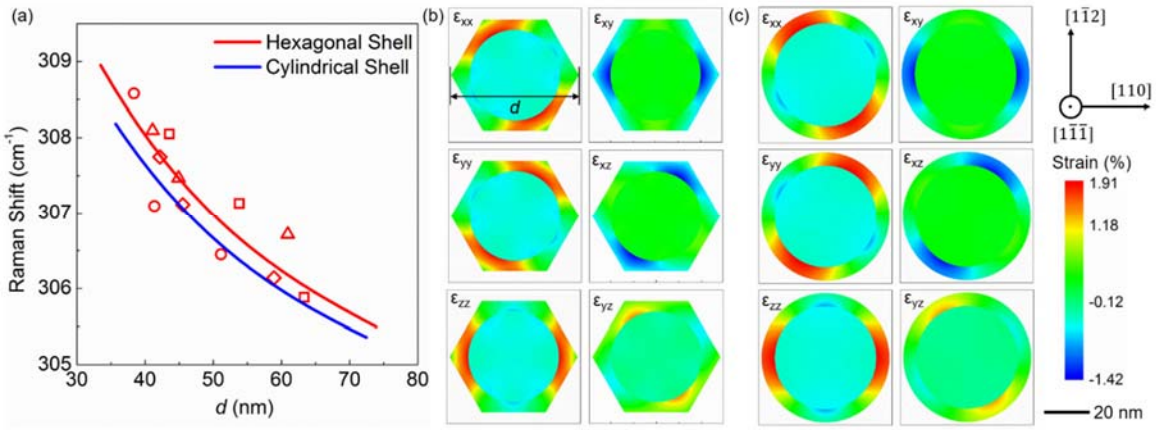

Figure 3.5 Strain distribution and strain-induced Raman mode shift of Ge−Si_xGe_{1-x} core-shell nanowire. (a) Diameter dependence of core Ge-Ge Raman modes measured along individual Ge−Si_xGe_{1-x} core-shell nanowires, where the nanowire tapering leads to a diameter change. The different symbols correspond to different nanowires. The solid lines indicate the calculated core Ge-Ge Raman modes using cylindrical and hexagonal shell cross-sections. (b) Calculated strain contour plots of Ge−Si_xGe_{1-x} core-shell nanowire with a hexagonal shell. (c) Calculated strain contour plots of Ge−Si_xGe_{1-x} core-shell nanowire with a cylindrical shell.

Figure 3.6(a) summarizes the diameter dependence of the core Si-Si Raman mode shift as a function of diameter acquired on individual Si−Si_xGe_{1-x} core-shell nanowires from growth C. The Si shell content, x = 0.68 is determined using the relative intensities of the shell Si-Si, Si-Ge, and Ge-Ge Raman modes. Using Fig. 3.3 data, we assign the <110> or <112> growth direction to individual nanowires, if their respective Raman spectrum exhibits two or three Si-Si modes, respectively. For both <110> and <112> oriented nanowires the core Si-Si Raman mode shift increases with diameter, consistent with a larger tensile strain at smaller diameters. Consistent with Fig. 3.3 data, Fig. 3.6(a) results show a larger shift for the core Si-Si Raman mode in <112> oriented nanowires. Two-dimensional contour plots of the elastic strain in <110>, and <112> oriented Si−Si_xGe_{1-x} core-shell nanowires, calculated using finite element simulations are shown in

Fig. 3.6(b), and 3.6(c), respectively. The elastic strain values of Fig. 3.6(b) and 3.6(c) are then converted into a corresponding Raman shift using Eq. (3.5), and are shown in Fig. 3.6(a) with solid lines. We note that the cubic elastic stiffness, phonon deformation potential and the nominal unstrained Si-Si Raman mode shift of 520.6 cm^{-1} may be less well-defined in <112> oriented Si-SiGe core-shell nanowires due to hexagonal phases [29]. This may account for the wider distribution of Si-Si Raman values in Fig 3.6(a) in <112> Si−Si_xGe_{1-x} core-shell nanowires.

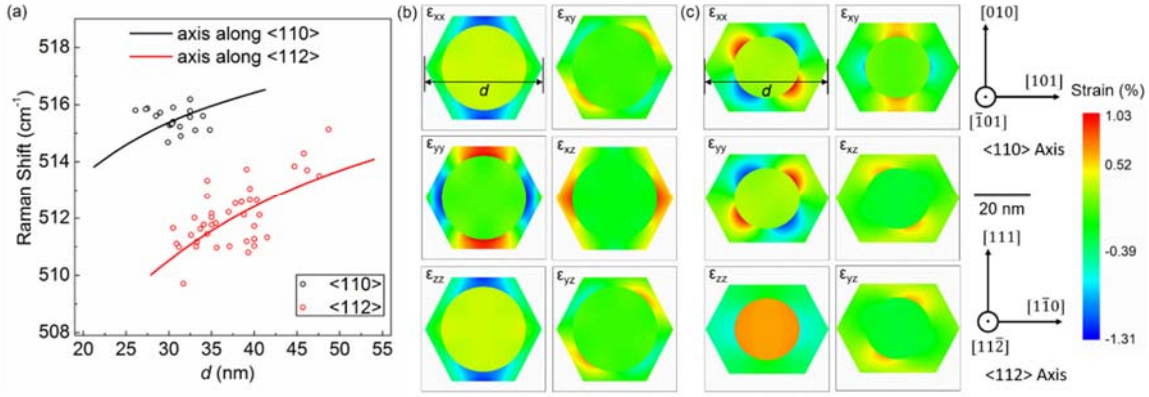

Figure 3.6 Strain distribution and strain-induced Raman mode shift of Si−Si_xGe_{1-x} core-shell nanowire. (a) Diameter dependence of core Si-Si Raman modes for the two types of Si−Si_xGe_{1-x} core-shell nanowires, with x=0.68. The symbols (solid lines) represent experimental data (calculations). (b) Calculated strain in <110> oriented, and (c) <112> oriented Si−Si_xGe_{1-x} core-shell nanowires. The strain profiles are distinct due to elastic constants anisotropy.

Chapter 4: Analysis of Core-Shell Nanowire Growth Result[3]

Lastly we address an interesting experimental observation, namely that the conformal CVD (shell) growth results in different shell thickness values, depending on the nanowire growth axis. Indeed, an examination of growths B-D of Table 2.2 shows that nanowires oriented along the <112> axis consistently have a larger shell thickness compared to nanowires from the *same* growth, that are oriented along the <110> axis. This is noteworthy because it implies that the same family of planes, i.e. {111} possess different growth rates depending on the nanowire growth axis during the *same* growth, namely under identical growth conditions. Furthermore, the difference in shell thickness becomes more pronounced as the shell growth temperature increases. An example is provided in Fig. 4.1(a-f), which shows HRTEM, FFT and STEM data from <110> and <112> oriented Si−Si_xGe_{1-x} nanowires (growth D). The different shell growth rates are presumably due to different surface hydrogen desorption rates [42], and suggest that hexagonal phases present in <112> oriented nanowires change the surface energies to stabilize facets along {113} planes, and also affect the hydrogen desorption rates.

Based on the findings of this study, a possible explanation for appearance of the seemingly energetically unfavorable shell morphology of <112> Si−Si_xGe_{1-x} core-shell nanowire could be that the hexagonal phases reduce the surface energy of {113} planes to favor them as shell facets. Previous experimental [43], and theoretical [44] studies have

[3] Chapter 4 is based on a prior publication, F. Wen, D.C. Dillen, K. Kim, E. Tutuc, Journal of Applied Physics 121 (23), 234302. F.W. performed the nanowire growth, TEM, Raman measurement and calculations, D.C.D. and K.K. help with facility training. F.W. and E.T. analyzed the data and co-wrote the paper.

also suggested that self-interstitials in {113} stacking faults lead to a reduction of the Si {113} surface energy, and to the presence of hexagonal phases [45, 46]. This may explain the unusual shell faceting of <112> oriented nanowires, at variance to a rectangular cross-section terminated by {111} and {110} planes, as expected based on energetic considerations [47, 48].

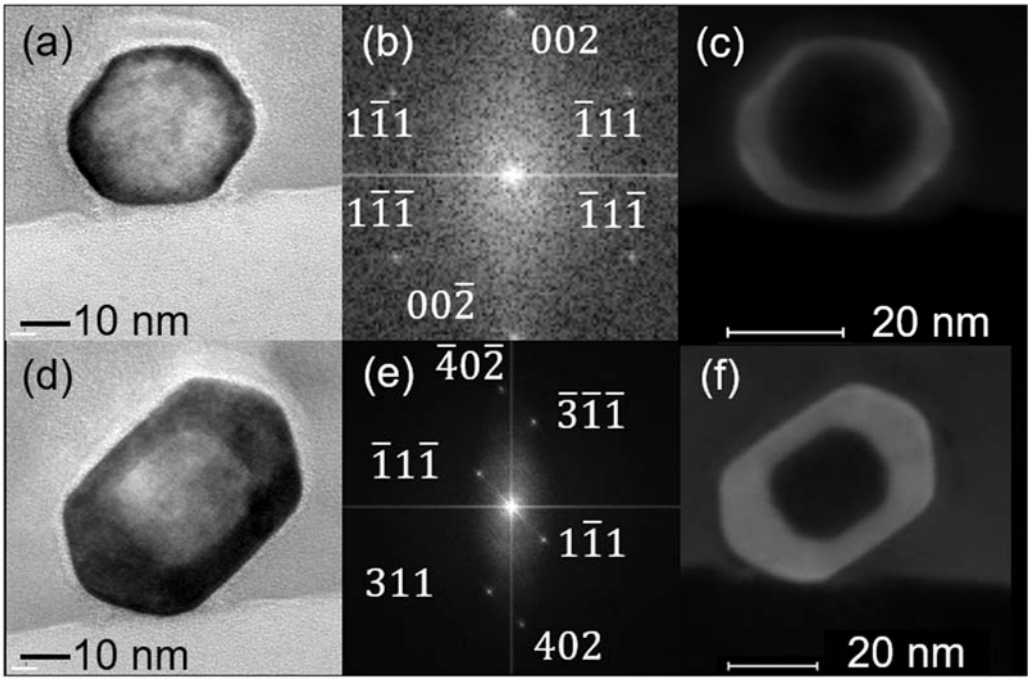

Figure 4.1 Shell thickness difference between <110> and <112> oriented Si−Si_xGe_{1-x} core-shell nanowires are exaggerated at higher shell growth temperature. (a-c) and (d-f) are cross-sectional HRTEM, FFT and STEM images for <110> and <112> oriented Si−Si_xGe_{1-x} nanowires (growth D), respectively.

We have also performed a Si−Si_xGe_{1-x} core-shell nanowire growth with a much thinner shell at a reduced shell growth temperature of 370 °C, with other growth conditions similar to growth B and C. Figure 4.2 shows the cross-sectional TEM images of two <110> oriented nanowires in this growth. The data shows that the Si_xGe_{1-x} shell still covers the

whole perimeter of the Si core and appears to be hexagonal, indicating the absence of island growth mode during the shell growth.

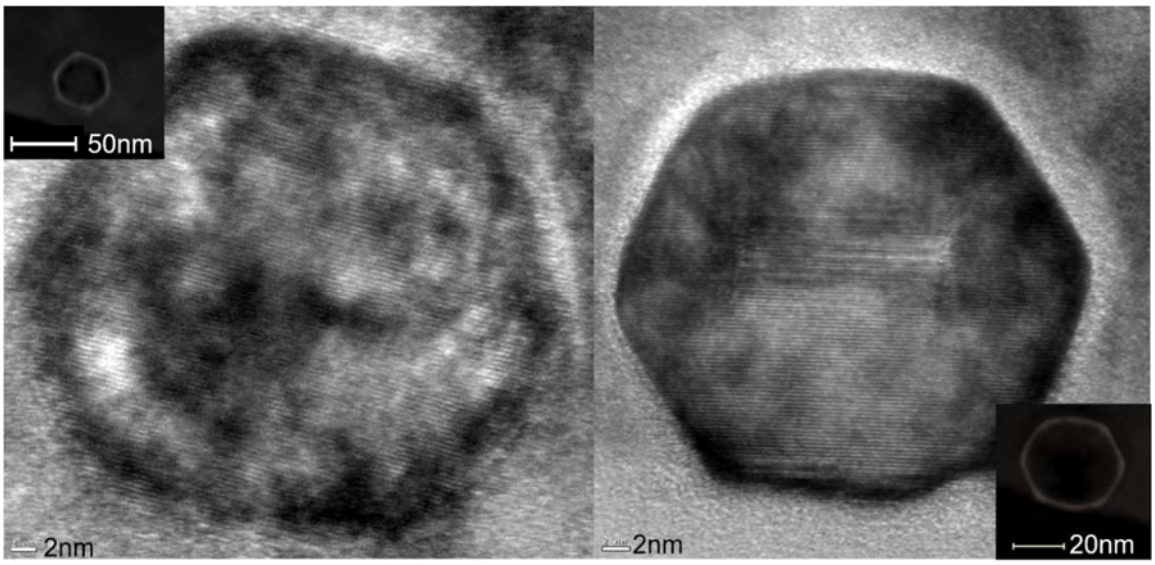

Figure 4.2 Cross-sectional TEM image of Si−Si_xGe_{1-x} core-shell nanowire with a very thin shell. Shell shape is still hexagonal and covers the complete perimeter of the core. Inset is the corresponding STEM image.

Chapter 5: Conclusion and Future Work

In conclusion, in this thesis we demonstrate that the shell morphology and Raman spectra of epitaxial Ge−Si_xGe_{1-x} and Si−Si_xGe_{1-x} core-shell nanowires are closely correlated. Cross-sectional TEM reveals two distinct hexagonal shell morphologies for Si−Si_xGe_{1-x} nanowires that correlate with the growth direction. Specifically, Si−Si_xGe_{1-x} nanowires growing along the <110> crystal axis are terminated by two {100}, and four {111} planes, while nanowires growing along the <112> crystal axis are terminated by two {111}, and four {113} planes. Remarkably, micro-Raman spectroscopy and cross-sectional TEM performed on the same nanowires reveal a direct correlation between the Raman spectra and shell morphology.

Future work that can be pursued includes more comprehensive study on how precursor partial pressure and temperature determine the growth direction of VLS nanowires, why defects associated with stacking faults are always embedded in <112> oriented Si nanowires, and the reason they can enhance the shell CVD deposition rate.

REFERENCE

[1] D. Wang, Q. Wang, A. Javey, R. Tu, H. Dai, H. Kim*, et al.*, "Germanium nanowire field-effect transistors with SiO[sub 2] and high-κ HfO[sub 2] gate dielectrics," *Applied Physics Letters,* vol. 83, p. 2432, 2003.

[2] V. Schmidt, H. Riel, S. Senz, S. Karg, W. Riess, and U. Gosele, "Realization of a silicon nanowire vertical surround-gate field-effect transistor," *Small,* vol. 2, pp. 85-8, Jan 2006.

[3] G. Liang, J. Xiang, N. Kharche, G. Klimeck, C. M. Lieber, and M. Lundstrom, "Performance Analysis of a Ge/Si Core/Shell Nanowire Field-Effect Transistor," *Nano Lett,* vol. 7, pp. 642-646, 2007.

[4] D. C. Dillen, K. Kim, E. S. Liu, and E. Tutuc, "Radial modulation doping in core-shell nanowires," *Nat Nanotechnol,* vol. 9, pp. 116-20, Feb 2014.

[5] B. Tian, X. Zheng, T. J. Kempa, Y. Fang, N. Yu, G. Yu*, et al.*, "Coaxial silicon nanowires as solar cells and nanoelectronic power sources," *Nature,* vol. 449, pp. 885-9, Oct 18 2007.

[6] L. J. Lauhon, M. S. Gudiksen, D. Wang, and C. M. Lieber, "Epitaxial core–shell and core–multishell nanowire heterostructures," *Nature,* vol. 420, pp. 57-61, 2002.

[7] W. Lu, J. Xiang, B. P. Timko, Y. Wu, and C. M. Lieber, "One-dimensional hole gas in germanium/silicon nanowire heterostructures," *Proc Natl Acad Sci U S A,* vol. 102, pp. 10046-51, Jul 19 2005.

[8] J. Nah, D. C. Dillen, K. M. Varahramyan, S. K. Banerjee, and E. Tutuc, "Role of confinement on carrier transport in Ge-Si(x)Ge(1-x) core-shell nanowires," *Nano Lett,* vol. 12, pp. 108-12, Jan 11 2012.

[9] D. C. Dillen, F. Wen, K. Kim, and E. Tutuc, "Coherently Strained Si-SixGe1-x Core-Shell Nanowire Heterostructures," *Nano Lett,* vol. 16, pp. 392-8, Jan 13 2016.

[10] S. Huang and L. Yang, "Strain engineering of band offsets in Si/Ge core-shell nanowires," *Applied Physics Letters,* vol. 98, p. 093114, 2011.

[11] M. M. Rieger and P. Vogl, "Electronic-band parameters in strainedSi1−xGexalloys onSi1−yGeysubstrates," *Physical Review B,* vol. 48, pp. 14276-14287, 1993.

[12] Y. Liang, W. D. Nix, P. B. Griffin, and J. D. Plummer, "Critical thickness enhancement of epitaxial SiGe films grown on small structures," *Journal of Applied Physics,* vol. 97, p. 043519, 2005.

[13] V. Schmidt, P. C. McIntyre, and U. Gösele, "Morphological instability of misfit-strained core-shell nanowires," *Physical Review B,* vol. 77, 2008.

[14] D. C. Dillen, K. M. Varahramyan, C. M. Corbet, and E. Tutuc, "Raman spectroscopy and strain mapping in individualGe-SixGe1−xcore-shell nanowires," *Physical Review B,* vol. 86, 2012.

[15] N. Søndergaard, Y. He, C. Fan, R. Han, T. Guhr, and H. Q. Xu, "Strain distributions in lattice-mismatched semiconductor core-shell nanowires," *Journal of Vacuum Science & Technology B: Microelectronics and Nanometer Structures,* vol. 27, p. 827, 2009.

[16] E. J. Jones, S. Ermez, and S. Gradecak, "Mapping of Strain Fields in GaAs/GaAsP Core-Shell Nanowires with Nanometer Resolution," *Nano Lett,* vol. 15, pp. 7873-9, Dec 9 2015.

[17] E. R. Hemesath, D. K. Schreiber, C. F. Kisielowski, A. K. Petford-Long, and L. J. Lauhon, "Atomic structural analysis of nanowire defects and polytypes enabled through cross-sectional lattice imaging," *Small,* vol. 8, pp. 1717-24, Jun 11 2012.

[18] T. Xu, J. P. Nys, A. Addad, O. I. Lebedev, A. Urbieta, B. Salhi*, et al.*, "Faceted sidewalls of silicon nanowires: Au-induced structural reconstructions and electronic properties," *Physical Review B,* vol. 81, 2010.

[19] H. Schmid, M. T. Björk, J. Knoch, H. Riel, W. Riess, P. Rice*, et al.*, "Patterned epitaxial vapor-liquid-solid growth of silicon nanowires on Si(111) using silane," *Journal of Applied Physics,* vol. 103, p. 024304, 2008.

[20] Y. J. Hyun, A. Lugstein, M. Steinmair, E. Bertagnolli, and P. Pongratz, "Orientation specific synthesis of kinked silicon nanowires grown by the vapour-liquid-solid mechanism," *Nanotechnology,* vol. 20, p. 125606, Mar 25 2009.

[21] J.-M. Zhang, F. Ma, K.-W. Xu, and X.-T. Xin, "Anisotropy analysis of the surface energy of diamond cubic crystals," *Surface and Interface Analysis,* vol. 35, pp. 805-809, 2003.

[22] D. D. D. Ma, C. S. Lee, F. C. K. Au, S. Y. Tong, and S. T. Lee, "Small-Diameter Silicon Nanowire Surfaces," *SCIENCE,* vol. 299, pp. 1874-1877.

[23] F. J. Lopez, E. R. Hemesath, and L. J. Lauhon, "Ordered Stacking Fault Arrays in Silicon Nanowires," *Nano Lett,* vol. 9, pp. 2774-2779, 2009.

[24] R. S. Wagner and R. G. Treuting, "Morphology and Growth Mechanism of Silicon Ribbons," *Journal of Applied Physics,* vol. 32, p. 2490, 1961.

[25] D. M. Bird, L. J. Clarke, R. D. King-Smith, M. C. Payne, I. I. Stich, and A. P. Sutton, "First principles calculation of the structure and energy of Si(113)," *Phys Rev Lett,* vol. 69, pp. 3785-3788, Dec 28 1992.

[26] M. E. Levinshtein, S. L. Rumyantsev, and M. S. Shur, "Properties of Advanced Semiconductor Materials: GaN, AIN, InN, BN, SiC, SiGe," ed: John Wiley & Sons, 2001, pp. 149-188.

[27] J. P. Dismukes, L. Ekstrom, and R. J. Paff, "Lattice Parameter and Density in Germanium-Silicon Alloys," *the Journal of Physical Chemistry,* vol. 68, pp. 3021-3027, 1964.

[28] M. I. Alonso and K. Winer, "Raman spectra ofc-Si1−xGexalloys," *Physical Review B,* vol. 39, pp. 10056-10062, 1989.

[29] F. J. Lopez, U. Givan, J. G. Connell, and L. J. Lauhon, "Silicon Nanowire Polytypes: Identification by Raman Spectroscopy, Generation Mechanism, and Misfit Strain in Homostructures," *ACS Nano,* vol. 5, pp. 8958-8966, 2011.

[30] A. Lugstein, M. Steinmair, Y. J. Hyun, G. H. Pongratz, and E. Bertagnolli, "Pressure-Induced Orientation Control of the Growth of Epitaxial Silicon Nanowires," *Nano Lett,* vol. 8, pp. 2310-2314, 2008.

[31] S. Ganesan, A. A. Maradudin, and J. Oitmaa, "A lattice theory of morphic effects in crystals of the diamond structure," *Annals of Physics,* vol. 56, pp. 556-594, 1970.

[32] E. Anastassakis, A. Pinczuk, E. Burstein, F. H. Pollak, and M. Cardona, "Effect of static uniaxial stress on the Raman spectrum of silicon," *Solid State Communications,* vol. 8, pp. 133-138, 1970.

[33] J. Menéndez, R. Singh, and J. Drucker, "Theory of strain effects on the Raman spectrum of Si-Ge core-shell nanowires," *Annalen der Physik,* vol. 523, pp. 145-156, 2011.

[34] R. Loudon, "The Raman effect in crystals," *Advances in Physics,* vol. 50, pp. 813-864, 2001.

[35] J. Wang, M. S. Gudiksen, X. Duan, Y. Cui, and C. M. Lieber, "Highly polarized photoluminescence and photodetection from single indium phosphide nanowires," *Science,* vol. 293, pp. 1455-1457, 2001.

[36] J. Qi, A. M. Belcher, and J. M. White, "Spectroscopy of individual silicon nanowires," *Applied Physics Letters,* vol. 82, p. 2616, 2003.

[37] J. S. Reparaz, A. Bernardi, A. R. Goñi, M. I. Alonso, and M. Garriga, "Composition dependence of the phonon strain shift coefficients of SiGe alloys revisited," *Applied Physics Letters,* vol. 92, p. 081909, 2008.

[38] E. Anastassakis, A. Cantarero, and M. Cardona, "Piezo-Raman measurements and anharmonic parameters in silicon and diamond," *Physical Review B,* vol. 41, pp. 7529-7535, 1990.

[39] F. Cerdeira, C. J. Buchenauer, F. H. Pollak, and M. Cardona, "Stress-Induced Shifts of First-Order Raman Frequencies of Diamond- and Zinc-Blende-Type Semiconductors," *Physical Review B,* vol. 5, pp. 580-593, 1972.

[40] P. M. Mooney, F. H. Dacol, J. C. Tsang, and J. O. Chu, "Raman scattering analysis of relaxed GexSi1−x alloy layers," *Applied Physics Letters,* vol. 62, p. 2069, 1993.

[41] J. C. Tsang, P. M. Mooney, F. Dacol, and J. O. Chu, "Measurements of alloy composition and strain in thin GexSi1−x layers," *Journal of Applied Physics,* vol. 75, p. 8098, 1994.

[42] J. J. Boland, "Role of hydrogen desorption in the chemical-vapor deposition of Si(100) epitaxial films using disilane," *Physical Review B,* vol. 44, pp. 1383-1386, 1991.

[43] D. J. Eaglesham, A. E. White, L. C. Feldman, N. Moriya, and D. C. Jacobson, "Equilibrium shape of Si," *Phys Rev Lett,* vol. 70, pp. 1643-1646, Mar 15 1993.

[44] J. Dabrowski, H. Mussig, and G. Wolff, "Atomic structure of clean Si(113) surfaces: Theory and experiment," *Phys Rev Lett,* vol. 73, pp. 1660-1663, Sep 19 1994.

[45] A. Parisini and A. Bourret, "Diamond hexagonal silicon phase and {113} defects Energy calculations and new defect models," *Philosophical Magazine A,* vol. 67, pp. 605-625, 1993.

[46] T. Y. Tan, H. Föll, and S. M. Hu, "On the diamond-cubic to hexagonal phase transformation in silicon," *Philosophical Magazine A,* vol. 44, pp. 127-140, 1981.

[47] S. A. Fortuna and X. Li, "Metal-catalyzed semiconductor nanowires: a review on the control of growth directions," *Semiconductor Science and Technology,* vol. 25, p. 024005, 2010.

[48] C.-P. Li, C.-S. Lee, X.-L. Ma, N. Wang, R.-Q. Zhang, and S.-T. Lee, "Growth Direction and Cross-Sectional Studyof Silicon Nanowires," *Advanced Materials,* vol. 15, pp. 607-609, 2003.

Vita

Feng Wen was born in Harbin, China on March 24, 1992. After graduating from Harbin No.3 Middle School in June 2010, he went on to study Electrical and Electronic Engineering at the University of Hong Kong in Hong Kong, China. In May 2014, Feng graduated with first class honor from HKU and a Bachelor of Engineering degree. In the following fall, he began his graduate studies in the Electrical and Computer Engineering Department of the University of Texas at Austin, studying solid state electronics. Feng joined the research group of Professor Emanuel Tutuc in September 2014 where he currently works with core-shell nanowire based electronic devices. After receiving his Master of Science degree in 2018, he intends to continue work towards a Ph.D. degree in Electrical and Computer Engineering at UT Austin.

Permanent email address: wenfeng5000@gmail.com

This thesis was typed by Feng Wen.